Journal of Materials Chemistry A

ROYAL SOCIETY OF CHEMISTRY

PAPER

View Article Online
View Journal

Open Access Article. Published on 02 March 2026. Downloaded on 3/2/2026 11:29:14 PM.
This article is licensed under a Creative Commons Attribution-NonCommercial 3.0 Unported Licence.

Check for updates

Cite this: DOI: 10.1039/d5ta10347a

Influence of Li-site dopants on phase stabilization, lithium distribution, and ionic conductivity in high-entropy Li-garnet solid electrolytes

Zhezhen Fu,* Neha Bulbule and Zhihao Jin

Garnet-type solid electrolytes are promising candidates for solid-state lithium batteries, yet their practical deployment is often limited by secondary phase formation, poor thermal stability during high-temperature processing, and overall conductivity. In this work, we systematically investigate the role of Li-site dopants in governing phase stability, secondary phase evolution, and Li-ion transport in the high-entropy garnet $Li_{6-x}A_xLa_3Zr_{0.5}Nb_{0.5}Ta_{0.5}Hf_{0.5}O_{12}$ (A = Al^{3+}, Fe^{3+}, Ga^{3+}, and Zn^{2+}). X-ray diffraction and microstructural analyses reveal strong dopant-dependent differences in thermal stability: while undoped, Al-, and Fe-doped compositions exhibit pronounced secondary phase formation under prolonged sintering, Ga- and Zn-doped garnets maintain single-phase cubic structures with excellent thermal robustness. Neutron diffraction refinements show that all compositions retain the cubic $Ia\bar{3}d$ framework but display distinct Li redistributions between tetrahedral 24d and octahedral 96h sites, directly controlling the topology of Li-ion migration pathways. Trivalent dopants enhance ionic conductivity by generating active octahedral vacancies and promoting Li-site disorder, whereas Zn^{2+} produces predominantly dopant-adjacent, mobility-suppressed vacancies despite improved phase stability. These results demonstrate that ionic conductivity in high-entropy garnets is governed not by total vacancy concentration or phase purity alone, but by the balance between thermal stability, secondary phase suppression, and active vacancy topology. This work establishes Li-site chemistry as a critical lever for simultaneously tuning phase stability and ionic transport in high-entropy garnet solid electrolytes.

Received 19th December 2025
Accepted 14th February 2026

DOI: 10.1039/d5ta10347a

rsc.li/materials-a

1 Introduction

Solid-state lithium batteries have emerged as one of the most promising technologies for achieving safer, high-energy-density energy-storage systems.[1–7] Among the wide range of solid electrolytes under development, garnet-type oxides have been particularly attractive because of their broad electrochemical stability window, compatibility with Li metal, and ionic conductivities that can reach the 10^{-4} to 10^{-3} S cm^{-1} range at room temperature.[3,8–11] The prototypical $Li_7La_3Zr_2O_{12}$ (LLZO) garnet hosts a three-dimensional migration network in which Li^+ moves through a series of interconnected tetrahedral (24d) and octahedral (96h) sites within the $Ia\bar{3}d$ framework.[12–14] Although stabilizing the cubic phase *via* aliovalent doping has been widely regarded as essential for fast ion transport, the fundamental origins of enhanced Li mobility have been the subject of substantial debate.[13–17]

Early interpretations often emphasized global descriptors such as Li stoichiometry, total vacancy concentration, or lattice expansion. However, neutron diffraction studies and theoretical analyses, particularly those by Chen *et al.* and Thompson *et al.* established a crucial refinement to this view.[13,14] These studies showed that the total number of Li vacancies is not the relevant carrier concentration; instead, ionic conductivity is controlled by how Li and vacancies distribute among the 24d and 96h sites. Vacancies on "active" 96h sites form the backbone of the percolating migration network, while vacancies adjacent to dopants become "influenced" sites that do not participate in long-range transport. This distinction helps to explain why some dopants markedly improve conductivity whereas others, despite generating more vacancies, suppress mobility. The conductivity of doped garnets therefore reflects a delicate balance between vacancy creation, local site distortions, and the preservation of a continuous 96h-24d-96h migration pathway.[13,15,18–21]

Recent developments in multicomponent or high-entropy Li-garnet have added new dimensions to this problem. Introducing multiple cations on the B-site (Zr/Nb/Ta/Hf) can stabilize the cubic phase through configurational entropy while simultaneously modifying the local Li potential landscape.[10,22–26] Our recent work on La-site doping within the high-entropy $Li_6La_3Zr_{0.5}Nb_{0.5}Ta_{0.5}Hf_{0.5}O_{12}$ (LLZNTH) system demonstrated that even isovalent substitution can lead to significant rearrangements in Li occupancy, altering the connectivity and

Mechanical Engineering, School of Science, Engineering and Technology, The Pennsylvania State University, Harrisburg, Middletown, PA, 17057, USA. E-mail: zwf5065@psu.edu

Open Access Article. Published on 02 March 2026. Downloaded on 3/2/2026 11:29:14 PM.
This article is licensed under a Creative Commons Attribution-NonCommercial 3.0 Unported Licence.

dimensionality of the Li^+ migration sublattice.[21,22,27] These observations highlight that dopants influence ionic transport not only by altering global structural stability, but by directly reshaping the Li-site energy landscape and redistributing Li between tetrahedral and octahedral positions. In high-entropy systems, where local disorder is inherently amplified, such effects become especially pronounced and can even outweigh penalties from secondary phases.[10,14,21] Although LLZO is widely recognized for its high ionic conductivity, its phase stability during high-temperature processing remains a critical challenge. Secondary phases such as $La_2Zr_2O_7$, $LaAlO_3$, or $LaFeO_3$ frequently emerge during sintering due to lithium loss, dopant segregation, or local compositional imbalance, and can severely disrupt Li-ion transport pathways.[17,18,21,28–30]

Building on this understanding, the present work investigates how aliovalent substitution on the Li-site modifies Li distribution and ionic conductivity in high-entropy garnets. Specifically, we examine Al^{3+}, Fe^{3+}, Ga^{3+}, and Zn^{2+} dopants,[14,28,29,31] each with distinct charge states, ionic radii, and electronic structures, to test how different dopant chemistries modulate vacancy topology and influence the fraction of active 96h sites. By combining neutron diffraction refinements with electrochemical impedance spectroscopy, we identify clear correlations between dopant-induced Li-site redistribution and the resulting transport properties. Our findings reveal that conductivity enhancement arises not from maximizing vacancy concentration but from maximizing the fraction of active, non-dopant-adjacent octahedral vacancies, in agreement with the mechanistic models proposed for LLZO but now demonstrated in a high-entropy garnet framework.[10,13,14]

This study provides a unified view that connects aliovalent doping, Li-site redistribution, and ionic transport in high-entropy garnets. By elucidating how specific dopants restructure the Li sublattice and identifying compositions that optimize active vacancy populations, we outline design principles for next-generation solid electrolytes that leverage both configurational entropy and targeted chemical substitution to engineer high-performance Li-ion conduction pathways.

2 Experiments

2.1. Sample fabrication

Following the chemical formulae listed in Table 1, the powders were prepared through a solid-state synthesis method.[21,22,32] Stoichiometric amounts of $LiOH \cdot H_2O$ with 10% excess (Li easily evaporates during synthesis and sintering, therefore, an excess amount was added, 98% minimum purity, Thermo Scientific), La_2O_3 (99.99% purity, Thermo Scientific, dried at 950 °C), ZrO_2 (99.9% purity, Inframat Advanced Materials), Nb_2O_5 (99.9% purity, Alfa Aesar), Ta_2O_5 (99.99% purity, Inframat Advanced Materials), HfO_2 (99%, Thermo Scientific), Al_2O_3 (99.99%, Inframat Advanced Materials), Fe_2O_3 (99.9%, Thermo Scientific), ZnO (99%, Thermo Scientific), and Ga_2O_3 (99%, MSE Supplies LLC) were ball milled for 1 hour using a zirconia milling tank and balls and isopropyl alcohol (IPA, >99.5%, VWR) as the liquid media on a shaker mill (SPEX 8000, SPEX SamplePrep). The mixture was dried at 105 °C, ground, and pressed into pellets. Calcination was conducted at 900 °C for 12 hours in air. Subsequent 2 hours of ball milling using zirconia milling media in IPA was performed on the shaker mill to reduce the particle size. The milled powders were uniaxially pressed into pellets under a pressure of ~60 MPa. The green pellets were surrounded by the same powder and placed in an alumina crucible with a lid to minimize the evaporation of Li during sintering. The pellets were sintered at 1200 °C for a duration of 2 to 8 hours. The heating and cooling rates were 3 °C min^{-1}. Both calcination and sintering were conducted in MgO crucibles to suppress Al_2O_3 diffusion into the Li-garnet during high-temperature heat treatment, which has been demonstrated to play a critical role in modifying garnet phase stability as well as its electrochemical performance.[33,34] In our previous work, Al_2O_3 crucibles were found to introduce trace Al that stabilized the garnet phase. Here, MgO crucibles were used to avoid unintended Al incorporation and isolate the effects of intentional Li-site doping.[21,22,35]

2.2. Sample characterization

Phases of the samples were characterized by X-ray diffraction (XRD, X'Pert PRO or Empyrean, Malvern Panalytical). Microstructures and element distributions of the sintered pellets were characterized by using a scanning electron microscope (SEM, Thermo Scientific Apreo 5, or Hitachi SU3900) equipped with an energy-dispersive X-ray spectrometer (EDS). The samples were also characterized by neutron powder diffraction (NPD) performed on VULCAN at the Oak Ridge National Laboratory.[36] The neutron diffraction patterns were refined through the GSAS

Table 1 Summary of LLZNTH-based samples, powder-phase constitution, phase stability after sintering, and room-temperature ionic conductivity

Sample composition	Short name	Powder phase	After sintering	Ionic conductivity ($\times 10^{-4}$ S·cm^{-1})
$Li_6La_3Zr_{0.5}Nb_{0.5}Ta_{0.5}Hf_{0.5}O_{12}$	None	Single cubic phase	Partial decompose	0.65
$Li_{5.4}Al_{0.2}La_3Zr_{0.5}Nb_{0.5}Ta_{0.5}Hf_{0.5}O_{12}$	Al0.2	Cubic + $LaAlO_3$	Partial decompose	1.54
$Li_{5.7}Al_{0.1}La_3Zr_{0.5}Nb_{0.5}Ta_{0.5}Hf_{0.5}O_{12}$	Al0.1	Single cubic phase	Partial decompose	0.60
$Li_{5.4}Fe_{0.2}La_3Zr_{0.5}Nb_{0.5}Ta_{0.5}Hf_{0.5}O_{12}$	Fe0.2	Cubic + $LaFeO_3$	Partial decompose	1.10
$Li_{5.7}Fe_{0.1}La_3Zr_{0.5}Nb_{0.5}Ta_{0.5}Hf_{0.5}O_{12}$	Fe0.1	Cubic + $LaFeO_3$	Partial decompose	1.68
$Li_{5.6}Zn_{0.2}La_3Zr_{0.5}Nb_{0.5}Ta_{0.5}Hf_{0.5}O_{12}$	Zn0.2	Single cubic phase	Stable	0.62
$Li_{5.4}Ga_{0.2}La_3Zr_{0.5}Nb_{0.5}Ta_{0.5}Hf_{0.5}O_{12}$	Ga0.2	Single cubic phase	Stable	1.47

 This journal is © The Royal Society of Chemistry 2026

Open Access Article. Published on 02 March 2026. Downloaded on 3/2/2026 11:29:14 PM. This article is licensed under a Creative Commons Attribution-NonCommercial 3.0 Unported Licence.

software package to obtain crystallographic structural parameters.[37]

To determine the ionic conductivity, Li-ion blocking silver paste was applied on the polished samples and fired at 700 °C for 0.5 hours to ensure a good interface. The ionic conductivity of each sample was determined by electrochemical impedance spectroscopy (EIS, SP-300, BioLogic) in the frequency range of 7 MHz to 1 Hz using the potentiostatic EIS model with a 100 mV amplitude at room temperature (~20 °C). The results were fitted using appropriate equivalent circuit models to obtain ionic conductivity. The conductivity was also determined at elevated temperatures up to 80 °C to obtain the activation energy.

3 Results and discussion

Fig. 1 presents the phase evolution of undoped LLZNTH processed in an MgO crucible at different sintering durations. The XRD pattern of the as-prepared powder shows diffraction peaks characteristic of the garnet structure, indicating that the garnet phase can be readily formed during the initial powder synthesis stage even without intentional lithium-site doping. No obvious impurity phases are detected at this stage within the resolution of XRD. To clarify this cubic phase stabilization behavior, reference samples of LLZO with and without Ta substitution are presented in Fig. S1. Undoped $Li_7La_3Zr_2O_{12}$ crystallizes in the tetragonal phase, whereas Ta substitution in $Li_{6.75}La_3Zr_{1.75}Ta_{0.25}O_{12}$ stabilizes the cubic structure, in agreement with prior studies. By analogy, the formation of the cubic phase in undoped LLZNTH is therefore attributed to the effect of aliovalent B-site substitution (Nb/Ta/Hf), which plays a role like that of conventional Ta doping in LLZO. This suggests that the cubic phase stabilization in LLZNTH originates from the combined effect of high-valence cation substitution on the Zr site, rather than requiring Li-site doping, enabling cubic phase formation already at the powder synthesis stage. In contrast, high-temperature sintering of the undoped material for extended durations (2–8 h) results in the gradual appearance of additional diffraction peaks associated with secondary phases including $La_2Zr_2O_7$ and La_3NbO_7. The intensity of these secondary-phase reflections increases with increasing sintering time, suggesting progressive phase decomposition or phase segregation during prolonged thermal treatment. Despite the use of an MgO crucible, which is commonly employed to mitigate lithium loss and interfacial reactions, the undoped composition remains thermodynamically unstable under extended sintering conditions.[33,34,38] These results demonstrate a clear distinction between powder-level phase formation and bulk sintering stability in undoped garnet compositions. While the garnet phase can be initially obtained, maintaining phase purity during high-temperature densification remains challenging without compositional modification. This observation highlights the intrinsic instability of the undoped lithium sublattice during prolonged thermal processing[39] and underscores the need for lithium-site doping to stabilize the garnet phase during sintering, as discussed in subsequent sections.

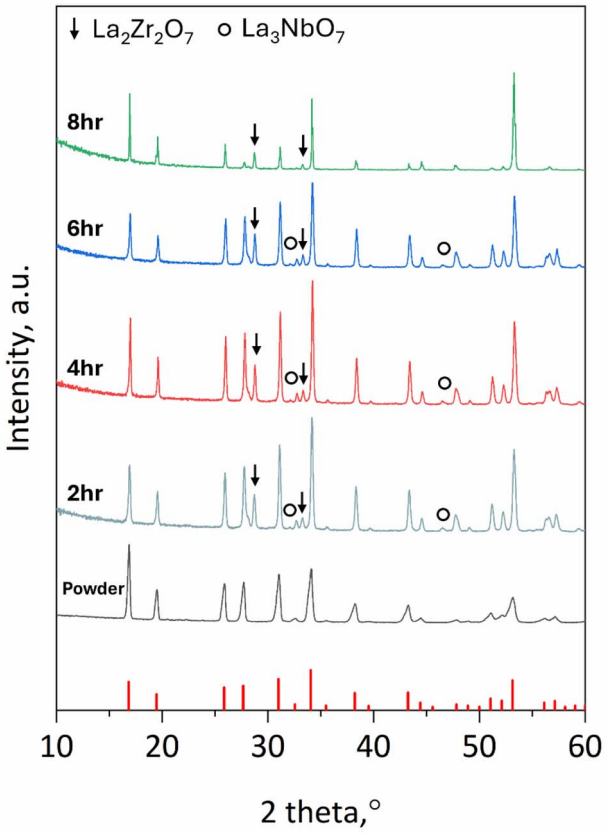

Fig. 1 XRD patterns of undoped $Li_6La_3Zr_{0.5}Nb_{0.5}Ta_{0.5}Hf_{0.5}O_{12}$ samples, including the as-prepared powder and pellets sintered at 1200 °C for 2, 4, 6, and 8 hours. The red reference pattern corresponds to the cubic Li-garnet phase.

Fig. 2 shows the phase evolution of Al0.2 (Al_2O_3 as the raw material) doped LLZNTH ($Li_{5.4}Al_{0.2}La_3Zr_{0.5}Nb_{0.5}Ta_{0.5}Hf_{0.5}O_{12}$) processed under identical conditions to the undoped sample. In contrast to the undoped composition (Fig. 1), the XRD pattern of the as-prepared powder already exhibits additional reflections corresponding to $LaAlO_3$. The emergence of this Al-rich secondary phase at the powder synthesis stage indicates that Al substitution at the lithium site alters the phase formation pathway and exceeds the effective solubility of Al in the garnet lattice, leading to early segregation prior to high-temperature sintering. Similar behavior has been reported for Al-doped LLZO, where Al incorporation beyond its solubility limit leads to the formation of $LaAlO_3$ rather than remaining in solid solution within the garnet lattice. Upon high-temperature sintering, secondary phases including $LaAlO_3$ and $La_2Zr_2O_7$ are observed, suggesting that excessive Al incorporation destabilizes the garnet lattice and promotes cation redistribution during thermal processing. In Al-doped LLZO, such phase evolution has been attributed to a combination of Al over-doping and lithium loss, which collectively drive the precipitation of $LaAlO_3$ and $La_2Zr_2O_7$ during sintering. To assess whether this behavior is primarily governed by Al dopant concentration, the Al content was reduced to 0.1, and the corresponding results are shown in Fig. S2. This comparison between Al0.2 and Al0.1 was designed to evaluate the solubility limit and concentration sensitivity of Al incorporation, rather than to establish an optimized doping

Open Access Article. Published on 02 March 2026. Downloaded on 3/2/2026 11:29:14 PM.
This article is licensed under a Creative Commons Attribution-NonCommercial 3.0 Unported Licence.

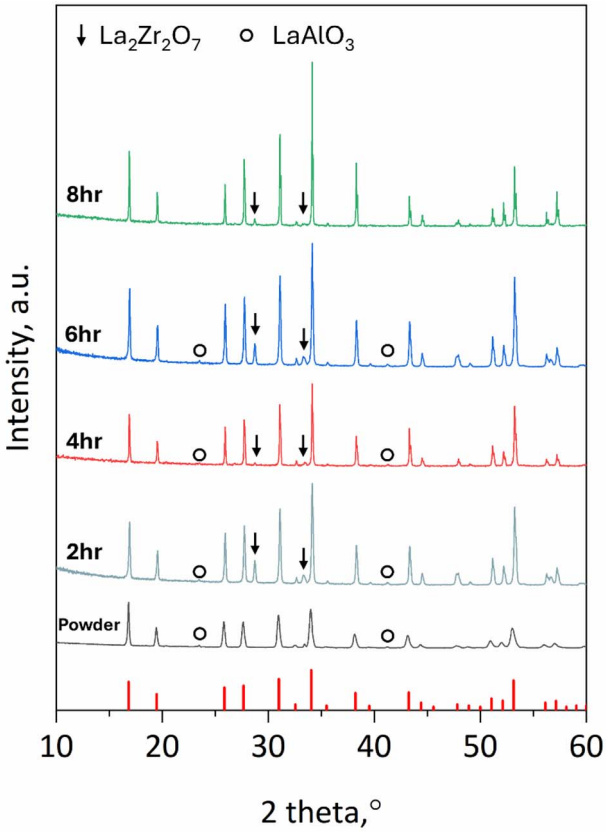

Fig. 2 XRD patterns of Al0.2 doped LLZNTH ($Li_{5.4}Al_{0.2}La_3Zr_{0.5}Nb_{0.5}Ta_{0.5}Hf_{0.5}O_{12}$) samples, including the as-prepared powder and pellets sintered at 1200 °C for 2, 4, 6, and 8 hours. The red reference pattern corresponds to the cubic Li-garnet phase.

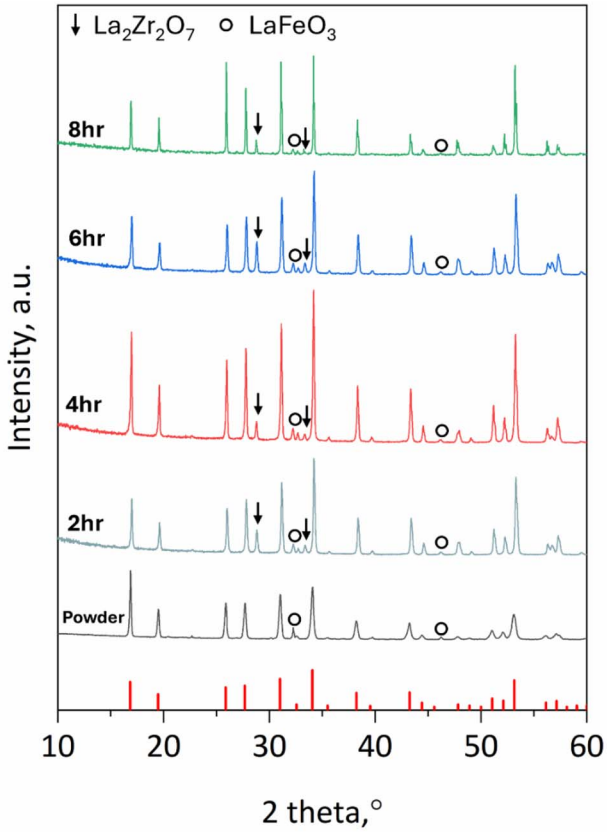

Fig. 3 XRD patterns of Fe0.2 doped LLZNTH ($Li_{5.4}Fe_{0.2}La_3Zr_{0.5}Nb_{0.5}Ta_{0.5}Hf_{0.5}O_{12}$) samples, including the as-prepared powder and pellets sintered at 1200 °C for 2, 4, 6, and 8 hours. The red reference pattern corresponds to the cubic Li-garnet phase.

window. At this reduced doping level, the $LaAlO_3$ phase is effectively suppressed in the as-prepared powder, consistent with Al contents below the reported solubility threshold in garnet electrolytes. However, pronounced $La_2Zr_2O_7$ reflections emerge during high-temperature sintering, with intensities increasing systematically with sintering time. This trend indicates that an Al content of 0.1 is insufficient to maintain the structural stability of the LLZNTH garnet under prolonged thermal exposure, likely due to progressive lithium depletion and subsequent decomposition pathways.[40] Notably, this behavior contrasts with samples processed in Al_2O_3 crucibles, where LLZNTH remains phase-stable even after extended sintering. This observation suggests that a gradual and continuous Al incorporation pathway, rather than direct compositional substitution, may be more effective in enhancing the thermal stability of the garnet lattice, potentially by avoiding local Al supersaturation and mitigating lithium loss during high-temperature processing.

Fig. 3 shows the phase evolution of Fe0.2 (Fe_2O_3 as the raw material) doped LLZNTH ($Li_{5.4}Fe_{0.2}La_3Zr_{0.5}Nb_{0.5}Ta_{0.5}Hf_{0.5}O_{12}$) processed under the same conditions as the undoped and Al-doped samples. Similar to the behavior observed for Al0.2 doping, the XRD pattern of the as-prepared powder exhibits additional reflections corresponding to the $LaFeO_3$ secondary phase, demonstrating that Fe substitution also alters the initial phase formation pathway and promotes early segregation of Fe-containing species. Upon high-temperature sintering, secondary phases, mainly including $LaFeO_3$ and $La_2Zr_2O_7$ persist throughout the entire sintering window, and their intensities do not diminish with extended dwell time. This indicates that Fe incorporation at a level of 0.2 strongly destabilizes the garnet lattice and triggers significant cation redistribution during thermal processing. To assess whether this instability is primarily associated with dopant concentration, the Fe content was reduced to 0.1 (Fig. S3), using the same comparative strategy applied to the Al-doped system, with Fe0.2 and Fe0.1 selected to probe the concentration-dependent phase stability and solubility behavior. At this reduced doping level, minor $LaFeO_3$ reflections are still detected in the as-prepared powder; however, these impurity peaks diminish upon high-temperature sintering, indicating improved incorporation of Fe into the garnet lattice at early sintering stages. With further extension of the sintering time beyond 6 h, secondary phases including $LaFeO_3$ and $La_2Zr_2O_7$ re-emerge and progressively intensify. This behavior differs from that observed for Al0.1 doping. At a reduced Fe content of 0.1, the garnet phase can be

Open Access Article. Published on 02 March 2026. Downloaded on 3/2/2026 11:29:14 PM.
This article is licensed under a Creative Commons Attribution-NonCommercial 3.0 Unported Licence.

effectively stabilized for sintering durations up to 6 h, indicating that moderate Fe incorporation is sufficient to support short-term phase stability. However, secondary phases ($LaFeO_3$ and $La_2Zr_2O_7$) for sintering over 6 hours suggest the onset of thermal decomposition under prolonged high-temperature exposure.[28] In contrast to Al0.1, which fails to stabilize the structure even at shorter sintering times, Fe0.1 exhibits an intermediate stabilization effect, likely associated with differences in cation valence, bonding characteristics, and site preference within the garnet lattice. It should be noted that the intensity of $La_2Zr_2O_7$ reflections does not evolve monotonically with sintering time. This behavior is consistent with prior *in situ* high-temperature diffraction studies of doped Li-garnet systems, which show that secondary phase evolution is governed by competing non-equilibrium processes, such as lithium volatilization and dopant redistribution, rather than a simple, monotonic decomposition pathway.[41] These results highlight the dopant-dependent nature of lithium-site substitution and demonstrate that both dopant chemistry and thermal budget must be carefully optimized to maintain phase stability during high-temperature processing.

Fig. 4 and 5 illustrate the phase evolution of Zn0.2 and Ga0.2 doped LLZNTH compositions. 0.2Zn doping results in a single-phase garnet structure already at the powder stage, with no detectable secondary phases. The garnet phase remains stable throughout prolonged sintering up to 8 h, demonstrating that Zn incorporation effectively suppresses phase decomposition and promotes thermal stability of the LLZNTH lattice. For Ga0.2 doping, minor secondary phases are observed in the as-prepared powder; however, these impurity reflections are eliminated upon sintering at 1200 °C, yielding phase-pure garnet pellets across the entire sintering window examined. This behavior is consistent with previous reports indicating that Ga incorporation into garnet electrolytes requires higher thermal activation to achieve full lattice incorporation. Once incorporated, Ga0.2 doped LLZNTH exhibits excellent phase stability, with no evidence of decomposition even after extended sintering durations. The contrasting phase evolution behavior among Al, Fe, Zn, and Ga systems highlights the critical role of dopant chemistry in governing lithium-site substitution and high-temperature stability. While Al and Fe doping exhibit narrow and processing-sensitive stability windows, Zn and Ga emerge as highly effective dopants for stabilizing the garnet structure at elevated temperatures. These results identify Zn and Ga as excellent lithium-site dopants capable of enhancing the thermal resilience of LLZNTH, offering valuable guidance

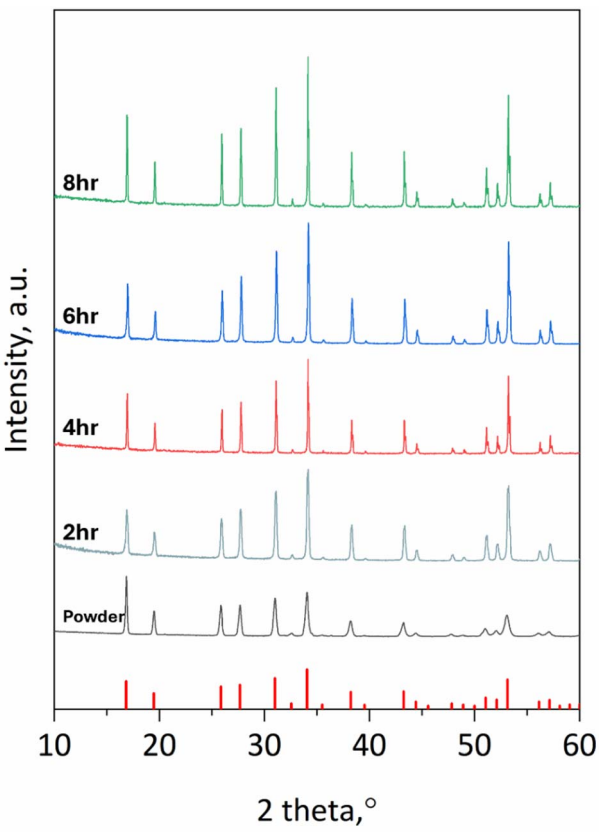

Fig. 4 XRD patterns of Zn0.2 doped LLZNTH ($Li_{5.6}Zn_{0.2}La_3Zr_{0.5}Nb_{0.5}Ta_{0.5}Hf_{0.5}O_{12}$) samples, including the as-prepared powder and pellets sintered at 1200 °C for 2, 4, 6, and 8 hours. The red reference pattern corresponds to the cubic Li-garnet phase.

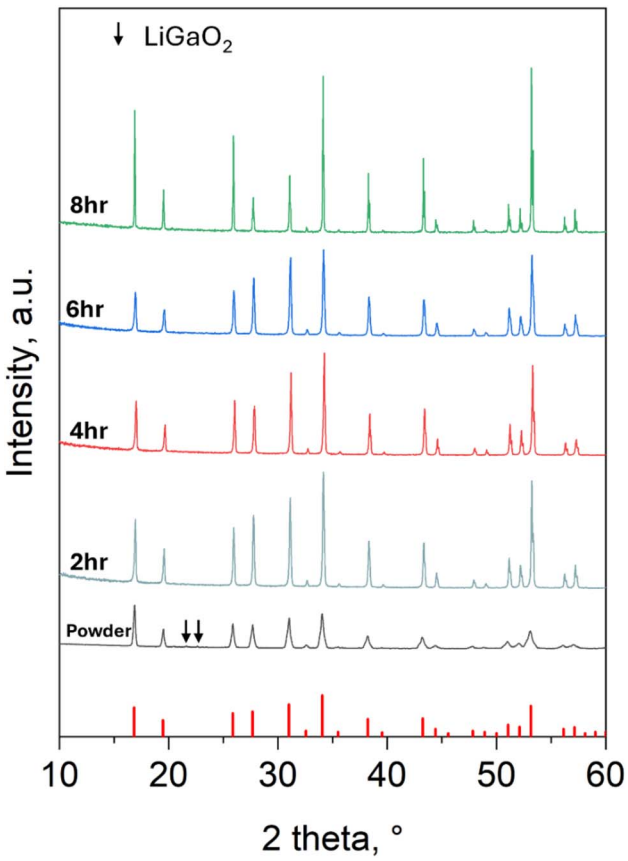

Fig. 5 XRD patterns of Ga0.2 doped LLZNTH ($Li_{5.4}Ga_{0.2}La_3Zr_{0.5}Nb_{0.5}Ta_{0.5}Hf_{0.5}O_{12}$) samples, including the as-prepared powder and pellets sintered at 1200 °C for 2, 4, 6, and 8 hours. The red reference pattern corresponds to the cubic Li-garnet phase.

Open Access Article. Published on 02 March 2026. Downloaded on 3/2/2026 11:29:14 PM.
This article is licensed under a Creative Commons Attribution-NonCommercial 3.0 Unported Licence.

for dopant selection in the design of high-performance high-entropy Li-garnet electrolytes.

Such XRD results demonstrate that (1) LLZNTH can form the cubic garnet phase even without Li-site doping, consistent with the behavior observed in conventional Ta-doped LLZO, where aliovalent Zr-site substitution is sufficient to stabilize the cubic framework at the powder stage. (2) In the absence of Li-site dopants, the garnet structure exhibits poor thermal stability and undergoes progressive decomposition during high-temperature sintering. (3) Al and Fe can be incorporated at the Li site but display limited compositional homogeneity. Their phase stability is highly sensitive to dopant concentration, and both systems eventually undergo thermal decomposition upon extended sintering. (4) Zn and Ga doped LLZNTH compositions exhibit a markedly different behavior. Both dopants enable uniform incorporation, yield single-phase garnet structures, and maintain excellent thermal stability throughout prolonged sintering. These observations highlight the strong dopant-dependence of Li-site substitution in LLZNTH and identify Zn and Ga as particularly effective stabilizers in high-entropy Li-garnet.

Fig. 6 compares the scanning electron microscopy (SEM) microstructure and energy-dispersive X-ray spectroscopy (EDS) elemental distribution of LLZNTH samples with different Li-site dopants after sintering for 2 hours at 1200 °C providing a consistent basis for evaluating early-stage densification behavior across all doped compositions. Clear differences in densification behavior and grain morphology are observed. The Al0.2 and Fe0.2 doped samples (Fig. 6a and b) exhibit relatively porous microstructures with fine, poorly developed grains, indicating limited densification at this early sintering stage. The grain sizes of these two samples are comparable, falling in the range of approximately 1–5 μm, and the fracture surfaces are dominated by transgranular fracture behavior. In contrast, the Zn0.2 doped sample (Fig. 6c) shows a much higher density with well-defined and more uniformly sized grains (∼1–3 μm), predominantly exhibiting intergranular fracture behavior. This microstructure suggests enhanced sintering kinetics and improved densification. The Ga0.2 sample (Fig. 6d) exhibits an extremely dense microstructure with very large grain sizes exceeding 100 μm. The presence of large-scale features and smooth surface contrast reflects pronounced grain coalescence behavior occurring during the sintering process. Elemental mapping further reveals pronounced differences in compositional homogeneity among the doped systems. For Al0.2 and Fe0.2 doping, localized enrichment of Al and Fe is evident, accompanied by corresponding variations in La and Zr distributions, indicating dopant segregation and local compositional inhomogeneity. These features are consistent with the secondary phases detected in XRD ($LaAlO_3$ and $La_2Zr_2O_7$ in the Al0.2 doped sample and $LaFeO_3$ and $La_2Zr_2O_7$ in the Fe0.2 doped sample), confirming that incomplete dopant incorporation and phase separation occur at early sintering stages. In contrast, Zn0.2 doped LLZNTH exhibits a highly uniform distribution of Zn as well as the host cations, consistent with its single-phase garnet structure observed by XRD. Similarly, Ga0.2 doped samples show relatively uniform elemental distributions at the micron scale, despite the presence of minor powder-stage secondary phases, which are eliminated upon sintering. Overall, the microstructural and compositional analyses in Fig. 6 corroborate the phase evolution trends identified by XRD. Dopants that promote uniform elemental distribution and enhanced densification, such as Zn and Ga, lead to stable single-phase garnet structures, whereas dopants associated with elemental segregation, such as Al and Fe, exhibit reduced thermal stability and secondary phase formation. These observations highlight the strong correlation between lithium-site dopant chemistry, microstructural development, and phase stability in LLZNTH systems.

Fig. 7 illustrates the microstructural evolution of Al0.2 doped LLZNTH as a function of sintering time. At short sintering durations (2–4 h, Fig. 7a and b), the sample exhibits a relatively fine-grained microstructure with limited grain growth and a uniformly distributed network of nanoscale to submicron pores. These features indicate limited densification and slow grain growth at the early stages of sintering. After 6 h of sintering (Fig. 7c), noticeable microstructural coarsening is observed. Grain boundaries become more defined, and grain size increases, accompanied by partial pore elimination. The number of pores is reduced compared with 2 and 4 hours of sintering but remains moderately porous, consistent with incomplete densification. A dramatic change occurs after 8 h of sintering (Fig. 7d). The microstructure becomes highly heterogeneous, with extensive large-scale cracking, abnormal grain coalescence, and the appearance of irregular textured regions. This degradation is consistent with the thermal decomposition suggested by XRD analysis, where secondary phases ($LaAlO_3$ and $La_2Zr_2O_7$) emerge and intensify with extended sintering. The onset of decomposition disrupts grain boundary structures, resulting in nonuniform microstructural development and the breakdown of the fine-grained morphology. A similar microstructure was also observed for the non-doped sample sintered at 1200 °C for 8 hours, as shown in Fig. S4. The SEM observations corroborate the XRD-identified phase instability of Al0.2 doping under prolonged thermal exposure. Al incorporation promotes initial grain growth but fails to maintain structural integrity at longer sintering times, where decomposition leads to severe microstructural heterogeneity.

Fig. 8 shows the microstructural evolution of Ga0.2 doped LLZNTH as a function of sintering time. In contrast to the significant microstructural changes observed in Al0.2 doped compositions, the Ga0.2 sample exhibits minimal morphological change across the entire 2 to 8 hours sintering window. At short sintering durations (Fig. 8a and b), the microstructure is already dense, with large, smooth grains and no evident intergranular porosity, indicating rapid densification and strong thermal stability at early stages. After 6 and 8 h of sintering (Fig. 8c and d), grain growth becomes more apparent. Large intragranular pores and very fine pores trapped within the grains begin to appear, a common feature associated with continued grain coarsening rather than phase instability. These isolated pores do not disrupt the overall microstructural uniformity and are consistent with the final-stage densification behavior of well-sintered ceramics. Additionally, no

 This journal is © The Royal Society of Chemistry 2026

Open Access Article. Published on 02 March 2026. Downloaded on 3/2/2026 11:29:14 PM.
This article is licensed under a Creative Commons Attribution-NonCommercial 3.0 Unported Licence.

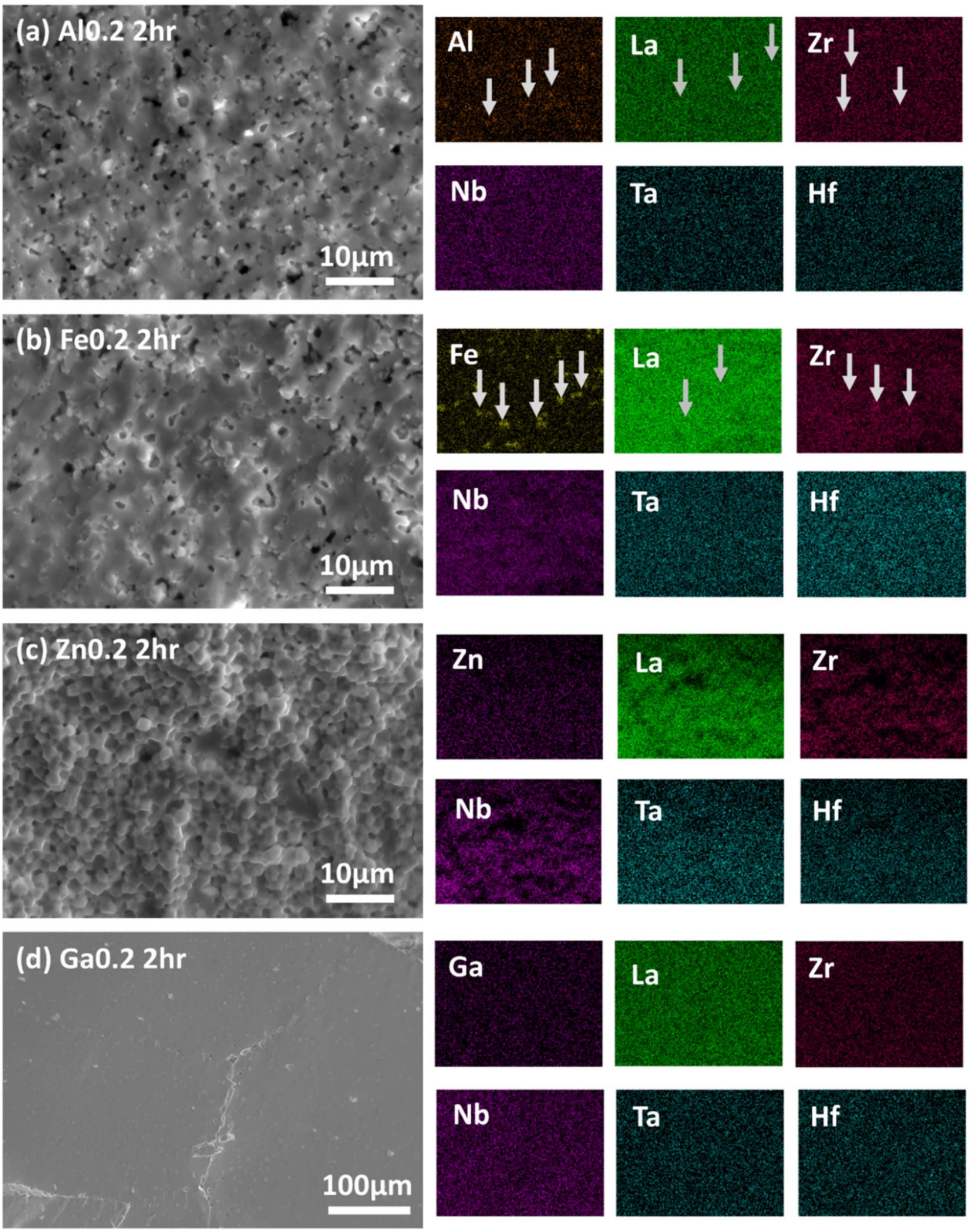

Fig. 6 Scanning electron microscopy images and corresponding energy-dispersive X-ray spectroscopy elemental mapping of LLZNTH samples sintered for 2 h with (a) Al0.2, (b) Fe0.2, (c) Zn0.2, and (d) Ga0.2 Li-site doping. Microstructural features and elemental distributions of the dopants and major constituent elements are compared to evaluate densification behavior and compositional homogeneity at early sintering stages.

Open Access Article. Published on 02 March 2026. Downloaded on 3/2/2026 11:29:14 PM.
This article is licensed under a Creative Commons Attribution-NonCommercial 3.0 Unported Licence.

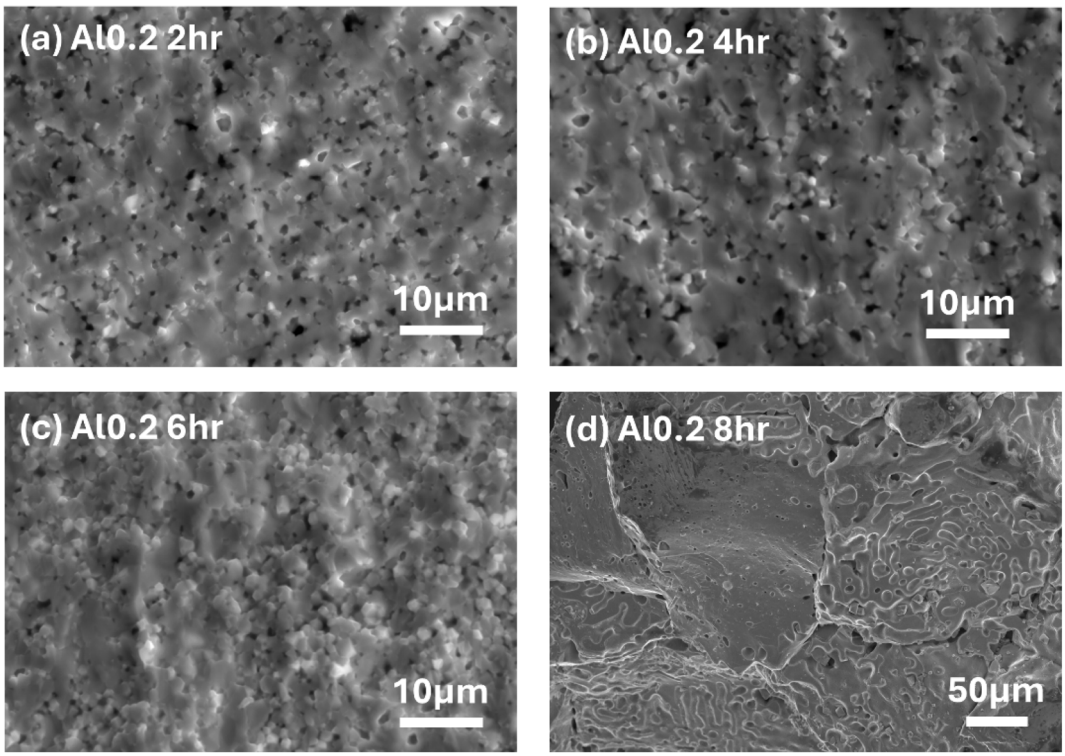

Fig. 7 SEM micrographs of Al0.2 doped LLZNTH sintered at 1200 °C for (a) 2 hours, (b) 4 hours, (c) 6 hours, and (d) 8 hours. Microstructural evolution with increasing sintering time highlights changes in grain morphology, pore distribution, and large-scale structural heterogeneity.

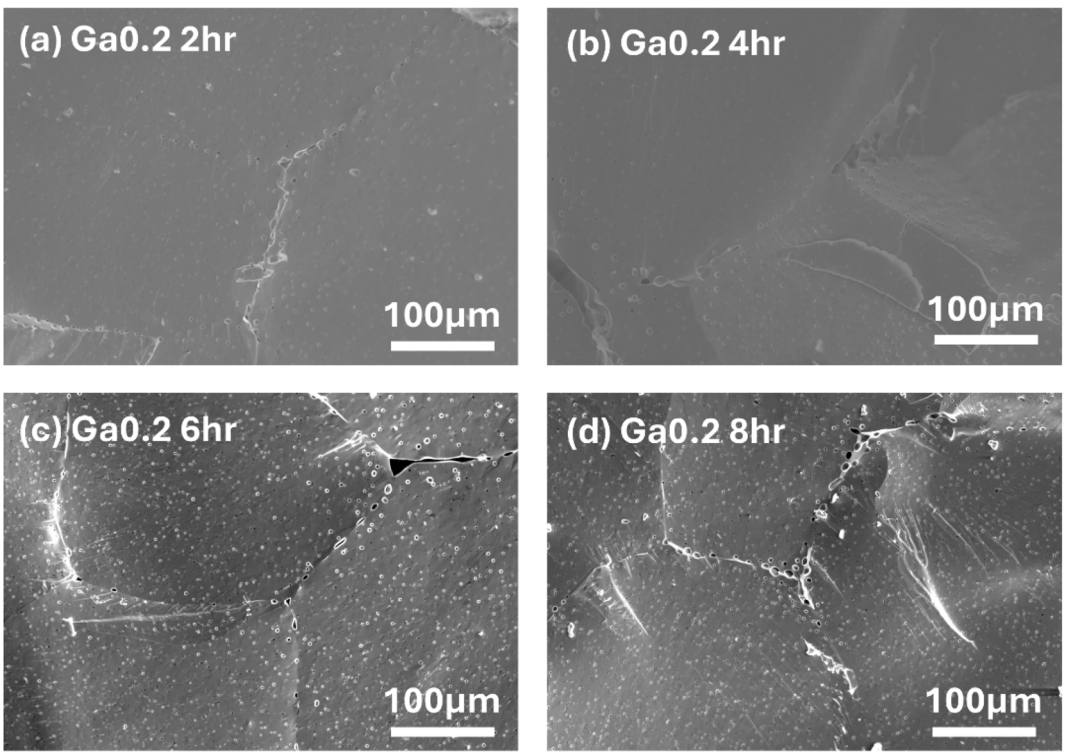

Fig. 8 SEM micrographs of Ga0.2 doped LLZNTH sintered at 1200 °C for (a) 2 hours, (b) 4 hours, (c) 6 hours, and (d) 8 hours. The evolution of the grain morphology and pore structure highlights the high thermal stability of Ga-doped LLZNTH under prolonged sintering conditions.

 This journal is © The Royal Society of Chemistry 2026

Open Access Article. Published on 02 March 2026. Downloaded on 3/2/2026 11:29:14 PM.
This article is licensed under a Creative Commons Attribution-NonCommercial 3.0 Unported Licence.

microstructural signatures of decomposition, such as abnormal grain contrast, secondary phase pockets, or large-scale texturing (as in the Al0.2 sample), are observed at any sintering duration. This observation aligns with XRD results, which show that Ga0.2 doped LLZNTH remains phase-pure throughout processing. The excellent thermal stability and minimal morphological degradation confirm Ga to be one of the most effective dopants for stabilizing the garnet phase during extended high-temperature sintering. SEM characterization was performed on Fe0.2 and Zn0.2 doped samples after prolonged sintering (8 h) as well, and the corresponding micrographs are provided in Fig. S5. Both systems exhibit noticeable microstructural coarsening and morphology evolution with extended sintering time. The Fe-doped sample shows increasing structural heterogeneity at longer dwell times, resembling the degradation trend observed in the Al-doped system, whereas the Zn-doped sample displays grain growth and localized pore development similar to the evolution seen in the Ga-doped composition. These observations suggest that microstructural changes under prolonged thermal exposure follow trends consistent with their respective phase stability behaviors.

Fig. 9a summarizes the room-temperature ionic conductivities of LLZNTH samples with different Li-site dopants as a function of sintering duration. For the undoped LLZNTH sample, measurable ionic conductivity (0.65×10^{-4} S cm^{-1}) is obtained only under the 2 h sintering condition. When sintering extends beyond 2 h, the conductivity drops below the detection limit. This sharp decline is consistent with the onset of thermal decomposition at elevated dwell times, as evidenced by the appearance of secondary phases in the XRD patterns (Fig. 1) and increased microstructural heterogeneity (Fig. S4). These results indicate that, in the absence of stabilizing dopants, prolonged high-temperature exposure destabilizes the garnet framework and disrupts Li-ion transport pathways, preventing reliable conductivity measurement.

Across the Al- and Fe-doped systems, the ionic conductivity exhibits a clear dependence on both dopant concentration and sintering duration. For the Al0.2 and Fe0.2 samples, conductivity increases from 2 h to 4 h (from 1.03 to 1.54×10^{-4} S cm^{-1} for Al0.2 and 0.84 to 1.10×10^{-4} S cm^{-1} for Fe0.2, respectively), which correlates with progressive densification and the reduction of residual porosity, as supported by SEM (Fig. 7). However, conductivity decreases after extended sintering (6 and 8 h), consistent with the onset of thermal decomposition and secondary-phase formation revealed by XRD. These structural changes degrade the continuity of Li-ion pathways, leading to diminished overall conductivity. The influence of dopant concentration is also evident. The Al0.1 sample displays uniformly low conductivity across all sintering durations, suggesting that insufficient Al incorporation fails to stabilize the conductive cubic framework, as confirmed by the mixed or weakly developed cubic features in XRD. In contrast, Fe-doping shows a more complex trend: the Fe0.2 sample exhibits suppressed conductivity, likely due to the emergence of Fe-rich secondary phases that impede transport. Meanwhile, Fe0.1 achieves one of the highest conductivities at 2 h of sintering (1.68×10^{-4} S cm^{-1}), which aligns with the single-phase garnet structure observed in Fig. S3 (2 and 4 h). With prolonged sintering time, although the garnet phase remains the majority phase, the ionic conductivity decreases, which correlates with the emergence of secondary phases observed in XRD and evolving microstructures. This degradation is likely driven by thermal decomposition and microstructural deterioration, suggesting that the conductivity drop is primarily governed by phase evolution and microstructural deterioration rather than lithium-site occupancy changes.[39,42]

The maximum conductivity of Ga-doped LLZNTH is 1.47×10^{-4} S cm^{-1}, which is comparable with Al and Fe, while only 0.62×10^{-4} S cm^{-1} for the Zn-doped sample. For these two samples, the conductivity shows relatively small variation

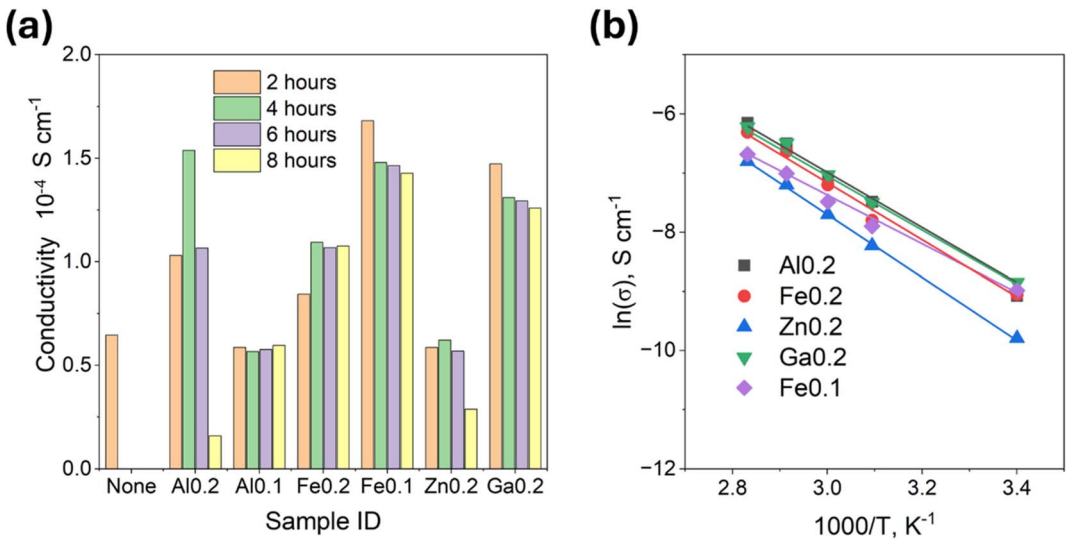

Fig. 9 (a) Room-temperature ionic conductivity of LLZNTH samples with various Li-site dopants (none, Al, Fe, Zn, and Ga) as a function of sintering duration (2, 4, 6, and 8 h at 1200 °C). (b) Arrhenius plots of selected samples sintered at 1200 °C (Al0.2: 4 h; Fe0.2: 4 h; Zn0.2: 4 h; Ga0.2: 2 h; Fe0.1: 2 h).

Open Access Article. Published on 02 March 2026. Downloaded on 3/2/2026 11:29:14 PM.
This article is licensed under a Creative Commons Attribution-NonCommercial 3.0 Unported Licence.

during the early sintering stages (2 h), consistent with the already dense and uniform microstructures seen in SEM. However, conductivity decreases slightly after prolonged sintering (4 to 8 h), likely due to over-sintering effects such as excessive grain growth and the formation of intragranular pores (as observed in Fig. 6 and 8). These microstructural changes can increase the effective blocking of Li-ion transport pathways, leading to a mild decline in conductivity despite the absence of phase decomposition.

As a summary, the conductivity trends in Fig. 9 demonstrate that dopant type and concentration strongly influence the stability and microstructural evolution of LLZNTH. Samples with appropriate dopant levels show conductivity improvements consistent with densification observed in SEM and phase stability indicated by XRD, whereas insufficient or excessive doping leads to suppressed conductivity that correlates with secondary-phase formation and microstructural degradation. Additionally, the conductivity of such samples is notably lower than that of LLZNTH processed using Al_2O_3 crucibles ($\sim$3 to 4 $\times$ 10^{-4} S cm^{-1}, no clear phase decomposition is observed under similar processing parameters).[21,22,42] This suggests that trace Al incorporation from Al_2O_3 crucibles may play a non-negligible role in tuning lithium stoichiometry and grain boundary transport, which has been shown to affect the electrochemical performance of garnet-type solid electrolytes.[34]

The activation energies (Fig. 9b; full impedance spectra and equivalent-circuit fits used for conductivity extraction are provided in Fig. S6) exhibit a clear dopant-dependent trend that correlates strongly with the measured room-temperature ionic conductivities. Samples with higher conductivity, such as Fe0.1, Al0.2, and Ga0.2, show relatively low activation energies (0.379 and 0.475 eV), indicating that Li-ion migration occurs through well-connected and energetically favorable pathways in these compositions. In contrast, samples with lower conductivity, including Zn0.2 and Fe0.2, exhibit higher activation energies (0.520 and 0.452 eV, respectively), reflecting increased barriers for Li-ion hopping. This behavior is consistent with their microstructural and phase characteristics: Zn0.2 displays limited densification, whereas Fe0.2 contains secondary phases that disrupt the garnet framework. The observed inverse relationship between conductivity and activation energy demonstrates that both dopant chemistry and microstructural stability play critical roles in governing Li-ion transport in LLZNTH garnets.

Neutron powder diffraction Rietveld refinements (Fig. 10 and S7) and corresponding results are summarized in Table S1. The NPD results confirm that all LLZNTH-based compositions adopt the cubic $Ia\bar{3}d$ garnet structure, yet exhibit pronounced differences in the distribution of Li between the tetrahedral 24d and octahedral 96h sites. This redistribution of Li, which modulates the topology and availability of mobile vacancies, emerges as the primary factor governing ionic conductivity across the series. When considered together with the ionic conductivity results in Fig. 9a, such a structure–transport relationship is consistent with the mechanistic framework established by Chen *et al.*[14,31] and Thompson *et al.*,[13] which showed that the total Li content alone does not define the carrier concentration; only Li and vacancies residing on specific "active" 96h octahedral sites contribute to long-range Li^+ migration. Consequently, the effective carrier concentration depends on how Li and vacancies partition between the 24d and 96h sublattices, and dopants influence conductivity predominantly by altering the fraction of active *versus* "influenced" (dopant-adjacent, mobility-suppressed) octahedral vacancies.[29] Across the Al-, Fe-, and Ga-doped compositions, NPD refinements indicate that aliovalent substitution drives Li-site repartitioning between the tetrahedral 24d and octahedral 96h sublattices. The dopants preferentially occupy the 24d site, while charge compensation is accommodated primarily through Li depletion from the 96h sublattice, thereby increasing the population of octahedral vacancies relevant to long-range Li^+ transport. Importantly, the resulting conductivity enhancement is governed not by the absolute Li occupancy on any single site, but by the fraction and connectivity of active 96h vacancies relative to dopant-adjacent, mobility-suppressed vacancies. The refined U_{iso} values for Li on 96h remain comparable across compositions; minor variations should be interpreted cautiously given correlations between occupancy and displacement parameters in Rietveld refinement. These results support an active-vacancy-network picture in which dopant chemistry controls whether newly created vacancies participate in a percolating migration network or become locally trapped. A schematic illustration summarizing this dopant-regulated vacancy topology and its impact on Li^+ migration pathways is provided in Fig. 11.

In the undoped LLZNTH sample, the high-entropy Zr-site framework stabilizes a robust cubic structure, yet neutron refinement indicates a Li content of approximately 6.49 f.u.$^{-1}$, slightly below the $\sim$6.5 mol threshold associated with maximized Li^+ mobility. The relatively high Li occupancy at the 24d site reduces the vacancy density on the 96h sublattice, thereby limiting the number of active vacancies available for diffusion. In agreement with the "Two-Site" model, this Li distribution results in only moderate conductivity despite the retention of a fully cubic structure. The introduction of trivalent dopants (Al^{3+}, Fe^{3+}, and Ga^{3+}) substantially alters this landscape. Across all Al-, Fe-, and Ga-doped compositions, neutron refinements show that charge-compensating Li depletion increases the overall vacancy concentration, while dopant incorporation at the 24d site promotes Li-site repartitioning and local disorder within the 96h sublattice. More importantly, the dopant-induced vacancies preferentially populate octahedral sites that are not adjacent to the dopant species, forming an extended network of active vacancies capable of supporting long-range Li^+ motion. The refined U_{iso} values for the 96h sites in Al0.2, Fe0.2, and Ga0.2 are consistent with substantial Li-site disorder and a broadened local energy landscape, although their absolute magnitudes should be interpreted cautiously due to parameter correlations in the refinement. Within this family, the Fe0.1 composition exhibits the highest conductivity, as it appears to strike an optimal balance: sufficient Fe^{3+} content to generate active vacancies, yet not so much that dopant-associated traps or vacancy clustering phenomena, previously reported for Fe-rich LLZO, begin to dominate. The absence of noticeable

Open Access Article. Published on 02 March 2026. Downloaded on 3/2/2026 11:29:14 PM.
This article is licensed under a Creative Commons Attribution-NonCommercial 3.0 Unported Licence.

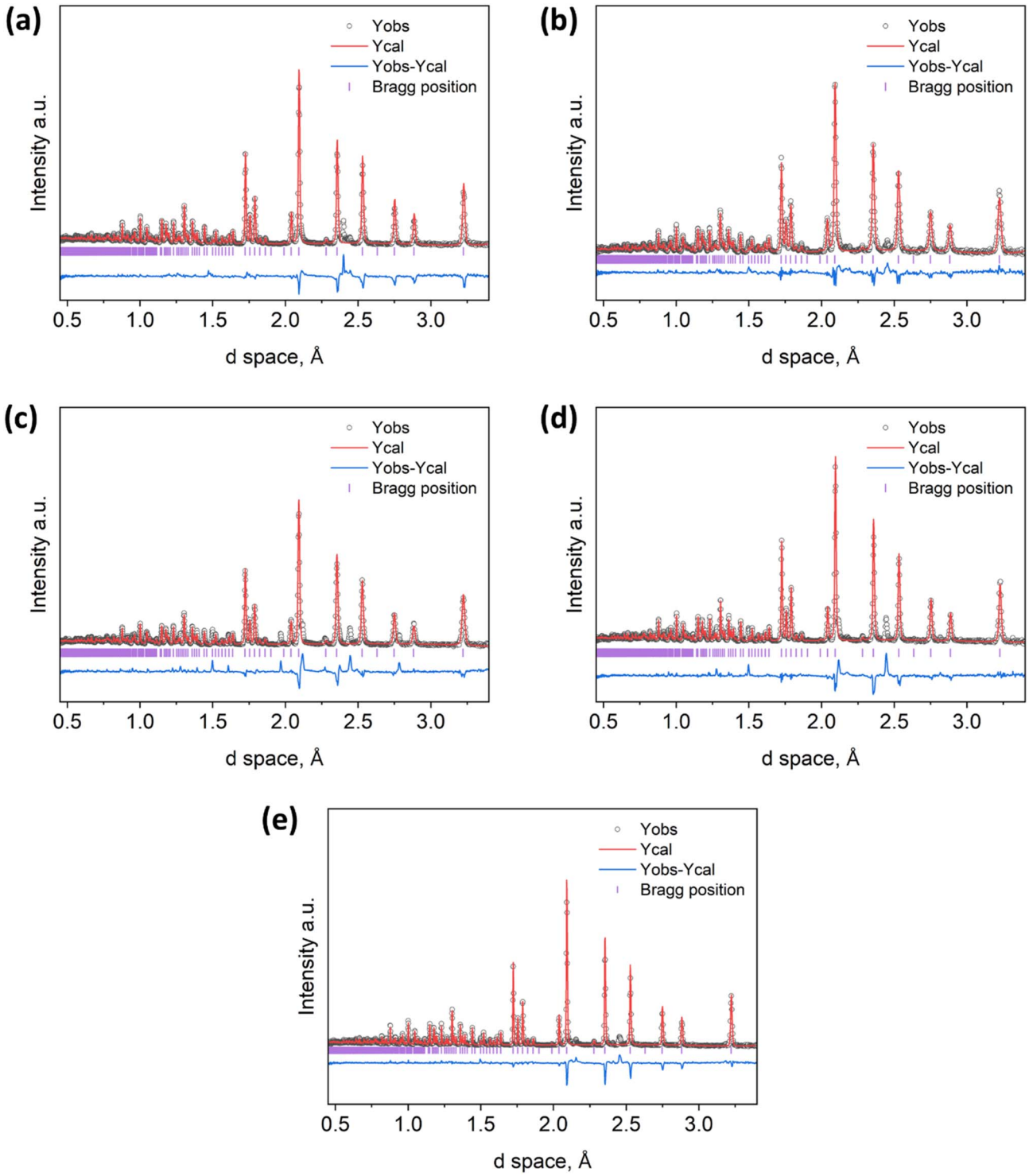

Fig. 10 Neutron powder diffraction Rietveld refinement profiles of LLZNTH samples with different Li-site dopants: (a) undoped, (b) Al0.2, (c) Fe0.2, (d) Zn0.2, and (e) Ga0.2.

secondary phases and the well-defined migration network in Fe0.1 align with the maximum conductivity predicted by Li-site occupancy curves derived by Thompson *et al.*[13] At higher dopant levels, particularly in Fe0.2 and Al0.2, the advantages of vacancy creation are offset by several detrimental effects. First, a larger fraction of vacancies becomes influenced sites, octahedral positions adjacent to dopant cations that exhibit reduced mobility due to strong local coulombic interactions. Chen *et al.* demonstrated that such dopant-adjacent vacancies can trap Li^+ for extended residence times, thereby diminishing their contribution to macroscopic transport.[14] This behavior is reflected in the neutron refinements and indicates that increasing

Open Access Article. Published on 02 March 2026. Downloaded on 3/2/2026 11:29:14 PM.
This article is licensed under a Creative Commons Attribution-NonCommercial 3.0 Unported Licence.

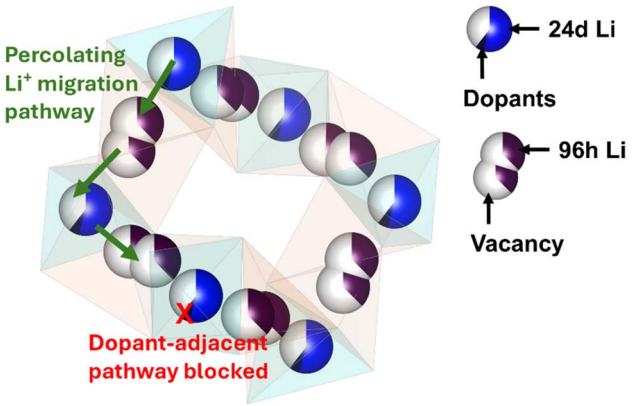

Fig. 11 Schematic illustration of Li^+ migration pathways and vacancy regulation in aliovalently doped LLZNTH garnets. Green arrows indicate percolating Li^+ migration pathways formed by interconnected octahedral (96h) vacancies. Aliovalent dopants preferentially occupy tetrahedral 24d (Li1) sites, while charge compensation through Li depletion from the 96h (Li2) sublattice generates vacancies that support long-range Li^+ transport. Vacancies adjacent to dopants exhibit reduced mobility and act as local blocking points (red cross), interrupting continuous pathways. Consequently, ionic conductivity is governed by the connectivity of active percolating vacancies rather than the total nominal vacancy concentration.

Fe or Al content increases Li occupancy within dopant-proximal 96h environments, thereby increasing the fraction of influenced sites. Second, both Fe and Al at elevated concentrations tend to form dopant-centered defect clusters, which locally distort the migration pathways. Third, microstructural degradation, specifically the onset of phase segregation and reductions in grain-boundary quality after prolonged sintering, further suppresses the effective conductivity. These factors rationalize why Fe0.2 exhibits a noticeably lower conductivity than Fe0.1, despite possessing a larger nominal vacancy concentration.

Zn^{2+} doping represents a mechanistically distinct case. Charge neutrality requires that each Zn^{2+} ion generate twice as many Li vacancies as a trivalent dopant, leading to a large total vacancy concentration. However, neutron refinements show that Zn preferentially occupies 24d and is associated with increased Li population in Zn-adjacent 96h environments, resulting in a high proportion of influenced vacancies. These configurations act as dead ends rather than components of the active vacancy network. Prior reports on Zn-LLZO have similarly shown that high vacancy concentrations do not necessarily translate into high conductivity when vacancy trapping dominates. Consequently, Zn0.2 displays one of the lowest conductivities in the series despite its seemingly favorable vacancy count. Ga0.2 constitutes an instructive contrast: Ga^{3+} generates a high active-vacancy concentration with minimal dopant-associated trapping. Ga-doped LLZO is often associated with enhanced Li disorder and favorable transport. In our refinements, Ga0.2 shows a redistribution of Li between 24d and 96h and an overall defect topology consistent with a high fraction of active vacancies; U_{iso} trends are supportive but should be interpreted cautiously due to parameter correlations. Combined with its excellent thermal stability and uniform microstructure, these structural characteristics yield a conductivity comparable to that of Al0.2 and only slightly below that of Fe0.1.

The conductivity trend (Fe0.1 > Al0.2 ≈ Ga0.2 > Fe0.2 ≫ Zn0.2 > Al0.1) emerges not from the lattice parameter, total Li content, or total vacancy concentration, but from the fraction of vacancies that remain active (*i.e.*, not adjacent to dopants), the extent of dopant-induced local distortion and trap formation, and the degree of Li-site disorder inferred from neutron occupancies and supported by U_{iso} trends. This mechanistic interpretation aligns directly with the predictive frameworks established by Chen *et al.* and Thompson *et al.*,[13,14] demonstrating that even in a high-entropy Zr-site environment, Li transport remains governed by the topology and quality of the octahedral vacancy network. Al, Fe, Zn, and Ga doped LLZNTH ($Li_{+x}A_xLa_3Zr_{0.5}Nb_{0.5}Ta_{0.5}Hf_{0.5}O_{12}$).

4 Conclusion

We investigated Li-site dopants (Al^{3+}, Fe^{3+}, Ga^{3+}, and Zn^{2+}) in the high-entropy garnet $Li_{+x}A_xLa_3Zr_{0.5}Nb_{0.5}Ta_{0.5}Hf_{0.5}O_{12}$ to reveal how dopant chemistry governs phase stabilization, Li distribution, and ionic transport and our conclusion is given below:

- All compositions retain the cubic $Ia\bar{3}d$ garnet structure, demonstrating that the high-entropy Zr-site matrix robustly stabilizes the cubic phase even under varied Li-site substitution.
- Neutron diffraction shows that different dopants induce distinct redistributions of Li between the 24d and 96h sites, directly influencing the formation and connectivity of Li^+ migration pathways.
- Trivalent dopants (Al^{3+}, Fe^{3+}, and Ga^{3+}) enhance cubic-phase stability and create active 96h vacancies, increasing Li-site disorder and enabling a continuous 3D migration network that boosts ionic conductivity.
- Zn^{2+} also preserves the cubic phase but produces predominantly dopant-adjacent (inactive) vacancies, suppressing mobility despite a high nominal vacancy concentration.
- The conductivity trend Fe0.1 > Al0.2 ≈ Ga0.2 > Fe0.2 ≫ Zn0.2 > Al0.1 correlates with the fraction of active (non-dopant-adjacent) octahedral vacancies, dopant-induced local distortion and trap formation, and Li-site disorder reflected in U_{iso} and refined occupancies.
- Fe0.1 achieves the highest ionic conductivity due to an optimal balance between vacancy creation and minimal dopant-centered trapping, illustrating the sensitivity of transport to vacancy topology.

In general, our findings demonstrate that ionic conductivity in high-entropy garnets is controlled not by total vacancies or phase purity alone, but by the spatial distribution and energetic accessibility of Li sites. This work establishes Li-site vacancy topology engineering as a powerful design principle for achieving simultaneous phase stabilization and high ionic conductivity in next-generation garnet solid electrolytes.

Conflicts of interest

There are no conflicts to declare.

 This journal is © The Royal Society of Chemistry 2026

Open Access Article. Published on 02 March 2026. Downloaded on 3/2/2026 11:29:14 PM.
This article is licensed under a Creative Commons Attribution-NonCommercial 3.0 Unported Licence.

Data availability

Additional data are available from the corresponding author upon reasonable request.

The data supporting the findings of this study are available within the article and its supplementary information (SI). Supplementary information: additional structural, microstructural, and electrochemical data that support the conclusions of this work. See DOI: https://doi.org/10.1039/d5ta10347a.

Acknowledgements

This material is based upon work supported by the National Science Foundation under Grant No. CMMI-2347492. A portion of this research used resources at the Spallation Neutron Source, a DOE Office of Science User Facility operated by the Oak Ridge National Laboratory. The beam time was allocated to VULCAN on proposal number IPTS-34906. Partial support by Penn State and Penn State Harrisburg seed grants is also acknowledged.

References

1 N. Nitta, F. Wu, J. T. Lee and G. Yushin, *Mater. Today*, 2015, **18**, 252–264.
2 M. R. Palacin and A. de Guibert, *Science*, 2016, **351**, 1253292.
3 S. Ramakumar, C. Deviannapoorani, L. Dhivya, L. S. Shankar and R. Murugan, *Prog. Mater. Sci.*, 2017, **88**, 325–411.
4 A. Manthiram, X. Yu and S. Wang, *Nat. Rev. Mater.*, 2017, **2**, 16103.
5 P. Albertus, V. Anandan, C. Ban, N. Balsara, I. Belharouak, J. Buettner-Garrett, Z. Chen, C. Daniel, M. Doeff, N. J. Dudney, B. Dunn, S. J. Harris, S. Herle, E. Herbert, S. Kalnaus, J. A. Libera, D. Lu, S. Martin, B. D. McCloskey, M. T. McDowell, Y. S. Meng, J. Nanda, J. Sakamoto, E. C. Self, S. Tepavcevic, E. Wachsman, C. Wang, A. S. Westover, J. Xiao and T. Yersak, *ACS Energy Lett.*, 2021, **6**, 1399–1404.
6 J. Hu, M. Lei, C. Zhu, B. Zhang and C. Li, *Adv. Funct. Mater.*, 2024, **34**, 2314044.
7 X. Nie, M. Lei, J. Hu and C. Li, *ACS Nano*, 2024, **18**, 30099–30112.
8 R. Murugan, V. Thangadurai and W. Weppner, *Angew Chem. Int. Ed. Engl.*, 2007, **46**, 7778–7781.
9 C. Wang, K. Fu, S. P. Kammampata, D. W. McOwen, A. J. Samson, L. Zhang, G. T. Hitz, A. M. Nolan, E. D. Wachsman, Y. Mo, V. Thangadurai and L. Hu, *Chem. Rev.*, 2020, **120**, 4257–4300.
10 Y. Zeng, B. Ouyang, J. Liu, Y.-W. Byeon, Z. Cai, L. J. Miara, Y. Wang and G. Ceder, *Science*, 2022, **378**, 1320–1324.
11 V. Thangadurai, S. Narayanan and D. Pinzaru, *Chem. Soc. Rev.*, 2014, **43**, 4714–4727.
12 V. Thangadurai, D. Pinzaru, S. Narayanan and A. K. Baral, *J. Phys. Chem. Lett.*, 2015, **6**, 292–299.
13 T. Thompson, A. Sharafi, M. D. Johannes, A. Huq, J. L. Allen, J. Wolfenstine and J. Sakamoto, *Adv. Energy Mater.*, 2015, **5**, 1500096.
14 Y. Chen, E. Rangasamy, C. Liang and K. An, *Chem. Mater.*, 2015, **27**, 5491–5494.
15 J.-F. Wu, E.-Y. Chen, Y. Yu, L. Liu, Y. Wu, W. K. Pang, V. K. Peterson and X. Guo, *ACS Appl. Mater. Interfaces*, 2017, **9**, 1542–1552.
16 Y. Zhu, J. G. Connell, S. Tepavcevic, P. Zapol, R. Garcia-Mendez, N. J. Taylor, J. Sakamoto, B. J. Ingram, L. A. Curtiss, J. W. Freeland, D. D. Fong and N. M. Markovic, *Adv. Energy Mater.*, 2019, **9**, 1803440.
17 T. Thompson, J. Wolfenstine, J. L. Allen, M. Johannes, A. Huq, I. N. David and J. Sakamoto, *J. Mater. Chem. A*, 2014, **2**, 13431–13436.
18 X. Liu, Y. Li, T. Yang, Z. Cao, W. He, Y. Gao, J. Liu, G. Li and Z. Li, *J. Am. Ceram. Soc.*, 2017, **100**, 1527–1533.
19 J.-F. Wu, W. K. Pang, V. K. Peterson, L. Wei and X. Guo, *ACS Appl. Mater. Interfaces*, 2017, **9**, 12461–12468.
20 S. Sarkar, C. Santos, J. Glenneberg, I. Bardenhagen, J. Schwenzel and V. Thangadurai, *Chem. Mater.*, 2024, **36**, 2685–2697.
21 C. Li, N. R. Giri, Y. Chen, F. A. Soto and Z. Fu, *ACS Appl. Mater. Interfaces*, 2025, **17**, 48267–48278.
22 Z. Fu and J. Ferguson, *J. Am. Ceram. Soc.*, 2022, **105**, 6175–6183.
23 S. Wang, X. Wen, Z. Huang, H. Xu, F. Fan, X. Wang, G. Tian, S. Liu, P. Liu, C. Wang, C. Zeng, C. Shu and Z. Liang, *Adv. Funct. Mater.*, 2025, **35**, 2416389.
24 C.-H. Kuo, P.-Y. Huang, A.-Y. Wang, H.-Y. Liu, H.-C. Cheng, C.-H. Lee, C.-R. Hsing, S.-Y. Chen, C.-H. Yeh, H.-J. Chen, H. Chen, W. Yin, J. Wu, C.-W. Pao, W. H. Kan, H.-Y. T. Chen and H.-Y. Chen, *J. Mater. Chem. A*, 2025, **13**(12), 8608–8618.
25 Y. Feng, L. Yang, Z. Yan, D. Zuo, Z. Zhu, L. Zeng, Y. Zhu and J. Wan, *Energy Storage Mater.*, 2023, **63**, 103053.
26 Y. Chen, T. Wang, H. Chen, W. H. Kan, W. Yin, Z. Song, C. Wang, J. Ma, W. Luo and Y. Huang, *Matter*, 2023, **6**, 1530–1541.
27 J.-y. Ock, M. Lehmann, C. Li, Y. Wang, H. M. Meyer III, A. P. Sokolov, Z. Fu and X. C. Chen, *J. Mater. Chem. A*, 2025, **13**, 24511–24521.
28 E. Anderson, E. Zolfaghar, A. Jonderian, R. Z. Khaliullin and E. McCalla, *Adv. Energy Mater.*, 2024, **14**, 2304025.
29 A. C. Moy, A. Manjón-Sanz, T. C. Caracciolo, M. V. Lobanov, G. M. Veith and J. Sakamoto, *J. Mater. Chem. A*, 2024, **12**, 28193–28210.
30 M. Abdulai, K. B. Dermenci and S. Turan, *Ceram. Int.*, 2021, **47**, 17034–17040.
31 Y. Chen, E. Rangasamy, C. R. dela Cruz, C. Liang and K. An, *J. Mater. Chem. A*, 2015, **3**, 22868–22876.
32 Z. Fu, D. McOwen, L. Zhang, Y. Gong, Y. Ren, J. E. Gritton, G. Godbey, J. Dai, L. Hu and E. Wachsman, *J. Am. Ceram. Soc.*, 2020, **103**, 5186–5195.
33 X. Huang, Y. Lu, H. Guo, Z. Song, T. Xiu, M. E. Badding and Z. Wen, *ACS Appl. Energy Mater.*, 2018, **1**, 5355–5365.
34 Y. Jiang, Y. Zhou, Z. Hu, Y. Huang and X. Zhu, *Ceram. Int.*, 2020, **46**, 3367–3373.
35 C. Li, N. R. Giri, Z. Jin, Y. Chen and Z. Fu, *Inorg. Chem.*, 2026, **65**(4), 2581–2590.

Open Access Article. Published on 02 March 2026. Downloaded on 3/2/2026 11:29:14 PM.
This article is licensed under a Creative Commons Attribution-NonCommercial 3.0 Unported Licence.

36 K. An, Y. Chen and A. D. Stoica, *MRS Bull.*, 2019, **44**, 878–885.
37 B. H. Toby, *Appl. Crystallogr.*, 2001, **34**, 210–213.
38 C. Chen, K. Wang, H. He, E. Hanc, M. Kotobuki and L. Lu, *Small*, 2023, **19**, 2205550.
39 A. Sharafi, C. G. Haslam, R. D. Kerns, J. Wolfenstine and J. Sakamoto, *J. Mater. Chem. A*, 2017, **5**, 21491–21504.
40 A. C. Moy, G. Häuschen, D. Fattakhova-Rohlfing, J. B. Wolfenstine, M. Finsterbusch and J. Sakamoto, *J. Mater. Chem. A*, 2022, **10**, 21955–21972.
41 Ø. Gullbrekken, K. Eggestad, M. Tsoutsouva, B. A. D. Williamson, D. Rettenwander, M.-A. Einarsrud and S. M. Selbach, *Inorg. Chem.*, 2025, **64**, 5856–5865.
42 Z. Fu and J. Ferguson, *Ceram. Int.*, 2023, **49**, 33981–33990.